Janus luminogens with bended intramolecular charge transfer: towards molecular transistor and brain imaging

Qian Wu[1,2], Junkai Liu[3], Youmei Li[1,2], Michelle M. S. Lee[3], Lianrui Hu[3], Panwang Zhou[4], Dong Wang[1,*] and Ben Zhong Tang[3,5,*]

[1]Center for AIE Research, Shenzhen Key Laboratory of Polymer Science and Technology, Guangdong Research Center for Interfacial Engineering of Functional Materials, College of Materials Science and Engineering, Shenzhen University, Shenzhen, 518060, China.

[2]Key Laboratory of Optoelectronic Devices and Systems of Ministry of Education and Guangdong Province, College of Optoelectronic Engineering, Shenzhen University, Shenzhen, 518060, China.

[3]Department of Chemistry, Hong Kong Branch of Chinese National Engineering Research Center for Tissue Restoration and Reconstruction, Institute of Molecular Functional Materials, The Hong Kong University of Science and Technology, Clear Water Bay, Kowloon, Hong Kong, 999077, China.

[4]Institute of Molecular Sciences and Engineering, Institute of Frontier and Interdisciplinary Science, Shandong University, Qingdao, 266235, China.

[5]Shenzhen Institute of Aggregate Science and Technology, School of Science and Engineering, The Chinese University of Hong Kong, Shenzhen, Guangdong 518172, China.

*e-mail: wangd@szu.edu.cn; tangbenz@ust.hk

Abstract

The ingenious construction of electron donor-acceptor (D-A) system has been proven to be the major trend for novel advanced-performance optoelectronic materials. However, the related development is undiversified and become stereotyped in recent years, and the explorations of new architecture with both prominent optoelectronic property and innovatively coined optoelectronic mechanism are appealing yet significantly challenging tasks. We herein exploit a series of novel Janus luminogens, namely TAOs, with unique charge separation in a simple five-membered mesoionic ring. TAOs having low molecular weight present efficient aggregation-induced red/near-infrared emission with up to 21.5% of fluorescence quantum yield. A new mechanism termed as bended intramolecular charge transfer (BICT) is proposed to understand the fluorescence behavior. It is experimentally demonstrated that TAOs exhibit great potential for the use as molecular transistor, and can be efficiently utilized in brain imaging straightforwardly through intravenous postinjection.

Introduction

In the last decades, the explosive advances of organic optoelectronic materials have been witnessed in organic light emitting diodes (OLEDs)[1,2], organic field-effect transistors (OFETs)[3,4], organic photovoltaic cells (OPVs)[5,6], sensors[7,8], and many other fields[9]. The construction of such materials with efficient charge transport is a fascinating target, which is usually realized by two strategies: (1) expansion of π-conjugation[10-12], and (2) enhancement of electron donating-accepting (D-A) strength[13,14]. The latter has been regarded as the most powerful tool in the development of novel high-performance organic materials by virtue of its great contributions in effectively narrowing the energy gap, enhancing the electron transfer, diversifying intermolecular interaction and adjusting molecular packing[15-20]. Scientists have spent much

effort on the exploration of desirable electron donors or acceptors, which were assembled by conjugated moiety as cross-bridges to construct the most popular D-π-A conjugated structure[21-25]. Nevertheless, the exploration of optoelectronic materials on the basis of these guidances has become stereotyped in recent years. And novel organic architecture with extraordinary optoelectronic properties and new optoelectronic principle remains barely exploited and supremely desirable.

Mesoionic compounds, as peculiar five-membered heterocycles bearing heteroatoms like O, N, S and P, were firstly defined by Baker, Ollis and Poole in 1949[26,27] and recently focused on bioortogonal click reaction in living system[28-30]. These structures are described as "*cannot be satisfactorily represented by any one covalent or polar structure and possesses a sextet of electrons in association with the five atoms of the ring*". It has been demonstrated that they possess planar and π-conjugated central ring with a side-chain whose α-atom is in the same plane which are both involving the delocalizations of electrons and charges[31-33]. Inspired by the strong charge separation of mesoionic compounds, we hypothesize it might be utilized for the construction of a unique family of mesoionic optoelectronic materials with high D-A strength in a single ring, rather than complicated modifications by long π-conjugation and bulky D/A units. More interestingly, intramolecular charge transfer in the ring rather than spatially segregated D-A structure in the excited state might provide a new perspective for in-depth understanding of optoelectronic mechanism. Given the circumstances, systemic evaluation on the optoelectronic characteristics of mesoionic compounds will be an appealing task.

Here, we reported a novel family of Janus luminogens on the basis of mesoionic fragment for the first time. Thiazol-3-ium-4-olate was utilized as a building block to construct 2,3,5-triphenylthiazol-3-ium-4-olate derivatives (TAOs) sharing red/near-infrared (NIR) aggregation-induced emission (AIE) characteristics. A meaningful mechanism termed as bended intramolecular charge transfer (BICT) was innovatively coined for elaborating the Janus structure, unusual optical properties and AIE behavior. Moreover, their optical properties can be effectively modulated by adjusting the substituent group at 3-position, indicating great potential for molecular transistor. TAOs having excellent biocompatibility were also exploited to serve as distinctive bioimaging agents for visualizing cell, bacteria, and particularly living mouse brain.

Results

Synthesis and characterization of TAO-TP

To validate the hypothesis, mesoionic compound 2,3,5-triphenylthiazol-3-ium-4-olate (TAO-TP) was facilely synthesized through a one-step reaction giving the yield of 89% (Fig. 1a). The structure of TAO-TP was fully characterized by NMR and high-resolution mass spectrometry (Supplementary Fig. 21). The strong and long-wavelength fluorescence emission in the solid of this simple structure whose molecular weight is only 329 $g \cdot mol^{-1}$ stimulated our interests in its optical properties. The UV-vis spectra were measured in various solvents (MeCN, DMSO, DMF, DCM, EA, THF, Dioxane, Et_2O and Toluene), as illustrated in Fig. 1b and Supplementary Fig. 1-2, these absorption maximums located in the range of visible light and red-shifted from 440 to 504 nm with the decrease of solvent polarity. The outcome diametrically opposed to that of twisted intramolecular charge transfer (TICT) system. More interestingly, THF solution of TAO-TP was barely emissive showing an extremely low fluorescence quantum yield (Φ_{soln} = 0.02%), while fluorescence emission was boosted upon adding water into the THF solution and achieve 28-fold enhancement in the case of 95% water fraction (Fig. 1c), in which uniform acicular morphology of TAO-TP with the size of 50 micrometers in the length was observed by fluorescence

microscope indicating the aggregate formation (Supplementary Fig. 3). In addition, the fluorescence quantum yield in solid state (Φ_{solid}) was determined to be 17.0% with the maximum emission wavelength at 624 nm (Supplementary Figure 1 and Table 1), which was about 85-fold higher than that in THF. These results clearly illustrated that TAO-TP is a red-emissive luminogen with typical AIE characteristics. The term, AIE, described a distinctive photophysical phenomenon was firstly put forward in 2001 by Tang group[34]. Nowadays, AIE luminogens (AIEgens) have drawn particular concerns which break through the limitations of traditional luminogens due to aggregation-caused quenching (ACQ) tendency[35], and undergo explosive developments in material science and biological science[36-38].

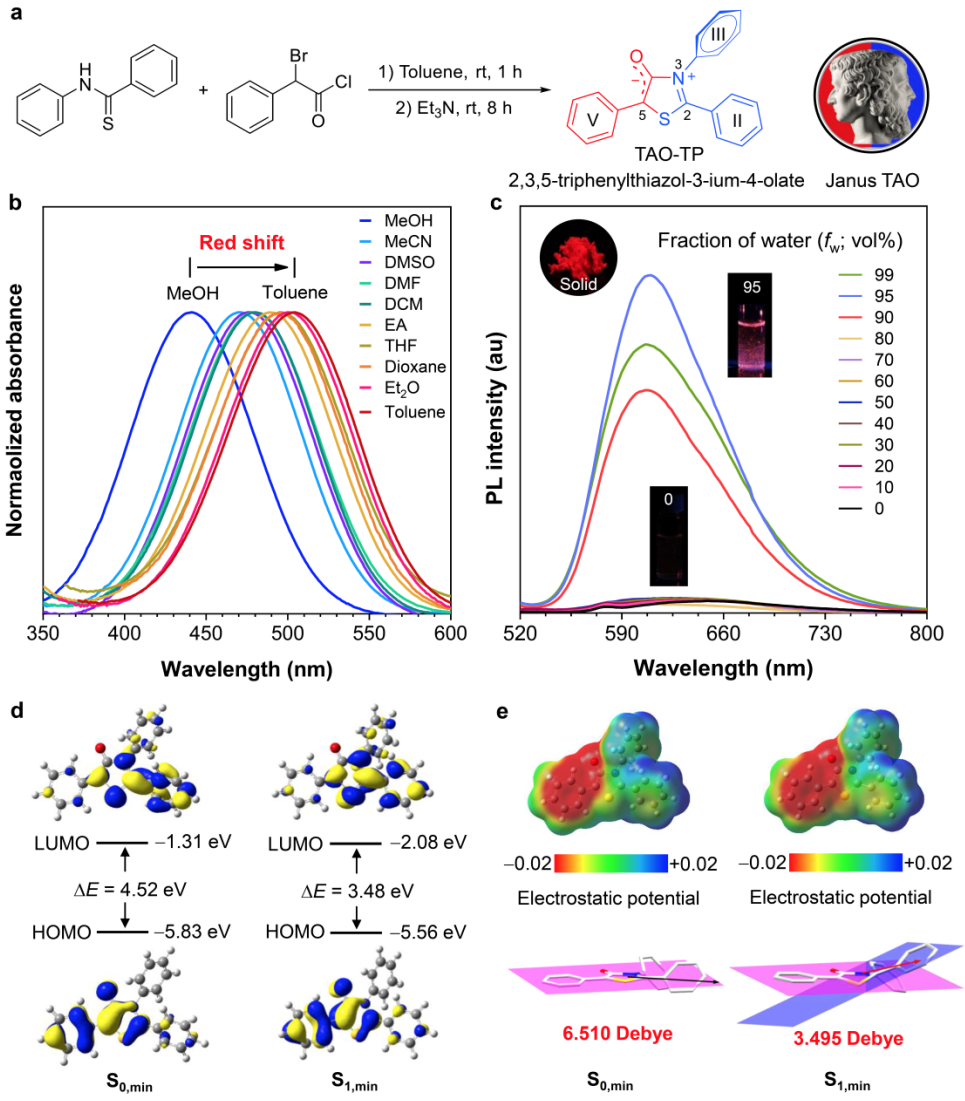

Figure 1. The synthetic route and basic characterizations of TAO-TP. a, Synthetic rout to TAO-TP and schematic diagram of Janus structure. **b**, Absorption spectra of TAO-TP (2×10^{-5} M) in different solvents. **c**, PL spectra of TAO-TP (2×10^{-5} M) in THF/water mixtures with different water fractions (f_w); λ_{ex} = 495 nm. Fluorescence photographs of TAO-TP solution with 0, 95% water faction and of TAO-TP powder irradiated by 365 nm UV light. **d**, The molecular orbital amplitude plots of HOMO and LUMO energy levels in the ground state (S_0) and excited state (S_1) calculated by using the (TD) M062X/6-31G (d, p) basis set. **e**, Simulated electrostatic potential and dipole moment in the ground state (S_0) and excited state (S_1) of TAO-TP.

Density functional theory (DFT) calculations were conducted for in-depth understanding the unique optical phenomenon of TAO-TP. As depicted in Figure 1d and 1e, the simulated electrostatic potentials and molecular orbital amplitude plots of TAO-TP in the ground state (S_0) and excited state (S_1) revealed that negative π-charge (related to highest occupied molecular orbital, HOMO) was mainly distributed in the left of central ting with O atom of the side-chain and ring V, while positive π-charge (related to lowest unoccupied molecular orbital, LUMO) was mainly delocalized in the other part of central ring and ring II. The energy gap between HOMO and LUMO was effectively reduced (from 4.52 eV in the S_0 to 3.48 eV in the S_1) which may be in a good accordance with the large stoke shift (152 nm). Moreover, the large simulated dipole moment of 6.510 Debye and segregated charges in the S_0 suggested the strong planar D-A structure at 2,5-positions of TAO-TP. The dipole moment in the S_1 was declined to be 3.495 Debye, which explained that the abnormal negative solvatochromism of TAO-TP was due to the better stabilizing effect of polar solvent on the ground state orbital[39]. On the basis of these dramatic results, we classified the TAO-TP as a "Janus" luminogen because it is possessed two antipodal charges in the same molecule like the mythological two-faced god who looked to the future and past in ancient roman religion.

TAO derivatives and related optical properties

According to the DFT calculation results, ring Ⅲ at 3-position of TAO-TP partially participated in charge distribution in HOMO and had flexible motions due to less steric hindrance of side-chain at 4-position. These features enabled the systematic investigations on regulation of optical properties by ring Ⅲ to be possible and significant. Hence, 12 derivatives of TAOs were synthesized with moderate to good yields and well characterized (Supplementary Fig. 22-33). A series of substituted TAOs with electron-donating (-OMe) or electron-withdrawing (-Br, -CF_3, -NO_2) groups at *para*-position of ring Ⅲ were prepared for evaluating the electronic effect (Fig. 2a). Several TAOs were also assembled by small alkyl groups substituted at the different positions (*ortho*, *meta* and *para*, Fig. 2b) or different-size substituted groups at the *ortho*-position (Fig. 2c) of ring Ⅲ to study the steric effect.

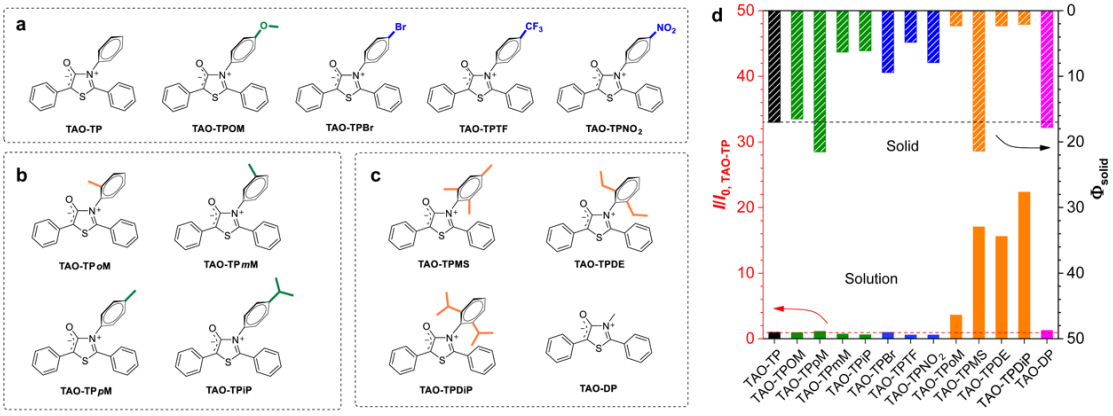

Figure 2. **Structures and optical properties of TAOs. a**, Structures of TAOs with different electron-donating and electron-withdrawing groups substituted at the *para*-position of ring Ⅲ. **b**, Structures of TAOs with small alkyl groups substituted at the different positions of ring Ⅲ. **c**, Structures of TAOs with different-size groups substituted at the *para*-position of ring Ⅲ and TAO-DP without ring Ⅲ. **d**, The relative emission intensity of TAOs ($I/I_{0,\ TAO\text{-}TP}$) in THF (down) and the quantum yield (Φ_{solid}) of TAOs in the solid state (up).

Optical properties of TAOs were investigated and summarized in Supplementary Table 1 and Fig. 4. Collectively, all those compounds were determined to be AIE-active showing bright aggregate emission in red/NIR region with up to 21.5% of fluorescence quantum yield in solid state (Supplementary Fig. 6-7). In the solution, whether electro-donating or electro-withdrawing groups only led to the emission wavelength shift, while the fluorescence intensity was slightly affected. Yet it was interesting to note that the fluorescence intensity gradually enhanced along with increasing steric hindrance (22.4 folds of TAO-TPDiP than TAO-TP, Fig. 2d). In the solid state, fluorescence efficiency presented by Φ_{solid} was susceptible to molecular packing. It was observed that twisted conformations resulted from asymmetric structure, high steric hindrance and electron-withdrawing groups caused fluorescence efficiency decrease (Fig. 2d). Combining with the results of melting point test and X-ray diffraction (Supplementary Fig. 5 and Table 2), it solidly demonstrated that the ring Ⅲ at 3-position indeed played a significant role in modulating the optoelectronic behaviors of TAOs, which was neglected in previous reports on luminous heterocycles.

Mechanism study

TAOs represent a new family of luminogens with AIE characteristics, thus the luminescence mechanism study is of vital significance. For this purpose, single crystal structure analysis, theoretical calculations and mechanism experiments were successively conducted. Firstly, the single crystal structure of TAO-TP*p*M was obtained by slow solvent evaporation and shown in Figure 4a-c and Supplementary Fig. 8. Both rings Ⅱ and Ⅴ showed coplanar conformations by small dihedral angles 33.56° and 12.49° with planar mosoionic central ring, while ring Ⅲ showed twisted conformations by dihedral angles 66.04°. The bond length of C-O bond was 1.23 Å, suggesting the double-bond feature. To do careful observations of molecular packing in different view, those intermolecular interactions between central ring and surrounding three phenyl groups (such as strong C-H···S and C-H···π), therein O atom and surrounding three phenyl groups of different molecules (strong C-H···O) were clearly presented by imaginary lines. These interactions resulted in well-ordered arrangement of TAO-TP*p*M with appropriate intermolecular distance (>3.73 Å) between two parallel planes to avoid the intermolecular π-π stacking. Moreover, the molecular conformation can be strongly rigidified to achieve effective restriction of molecular motions which was beneficial for boosting the excited-state energy dissipation from radiative decay pathway, consequently enhancing the emission efficiency in aggregation state.

The electron vibration couple analysis of TAO-TP*p*M was further investigated through combined quantum mechanical and molecular mechanical (QM/MM) simulations to illustrate the refined structural changes upon excitation respectively in the solution and crystal[40,41]. Based on the crystal structure of TAO-TP*p*M, the intermolecular packing effect is incorporated through electrostatic interaction modeled by a force field. The reorganization energies versus the normal mode frequencies of TAO-TP*p*M in both gas and crystal phases were plotted in Fig. 3d-f. The results revealed that the total reorganization energy was 6619 cm^{-1} in the gas phase indicating vigorous molecular motions, whereas it significantly decreased to 1984 cm^{-1} in the crystal phase. The energy decrease was dominated by the suppression of the low-frequency (<400 cm^{-1}) vibration, in which the remarkable decrease of the dihedral angle from 70% in the gas phase to 29% in the crystal phase made a vital contribution. Further detailed classification analysis on the central ring and outer phenyl rings showed the dominant component of the dihedral angle associated with the motions in the central five-membered ring, from 54.9% in the gas phase to 7.6% in the crystal phase (Fig. 3e). Interestingly, it was different from the common AIE systems containing

five-membered heterocycles, in which the phenyl-ring motions at the 2- and 5-positions were always crucial[40]. To clarify the relationship between the energy dissipation and the molecular structure, the structural change between the ground state and excited state was further assessed. As depicted in Fig. 3f, an obvious conformation bending of planar central ring occurred upon excitation in the gas state and further prompted the warping of surrounding phenyl rings. On the contrary, such bending was quite negligible in the crystal state. These results suggested that the excited-state energy dissipation was easily suppressed via restriction of the bend in the central ring by aggregates formation.

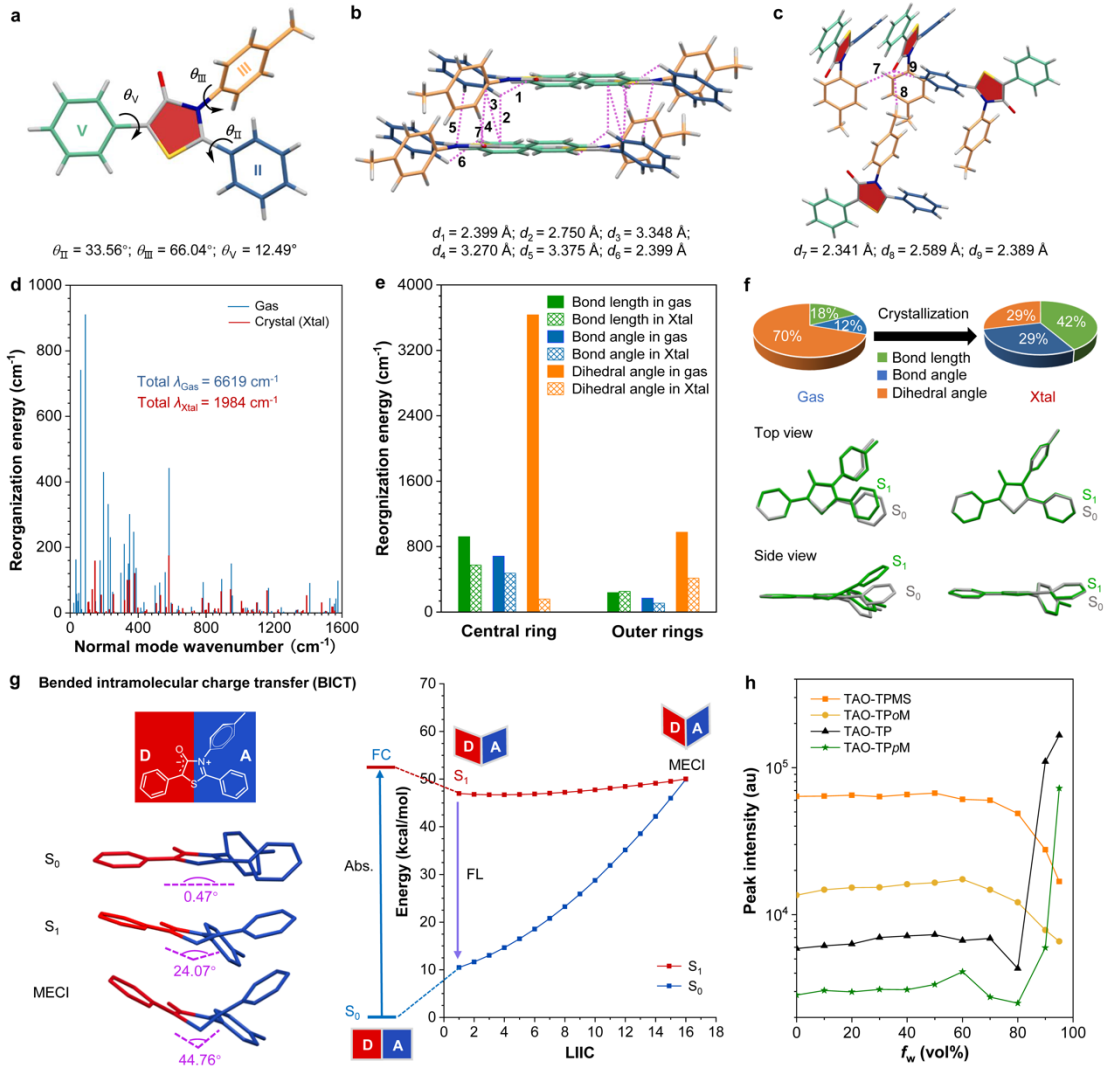

Figure 3. Mechanism for AIE characterization of TAOs. a, Single-crystal structure of TAO-TP*p*M. **b and c**, The molecular packing and intermolecular interactions in crystal of TAO-TP*p*M. **d**, QM/MM simulation for TAO-TP*p*M calculated by using the ONIOM((TD)-M062X/6-31G(d,p):UFF) basis set. Calculated reorganization energies versus the normal-mode frequencies of TAO-TP*p*M molecule in the gas phase (blue) and the solid phase (red). **e**, Classified contributions to the total reorganization energy from central ring and outer rings of TAO-TP*p*M in the gas phase and the solid phase. **f**, Contributions to the total reorganization energy from bond length, bond angle and dihedral angle of TAO-TP*p*M in the gas phase and the solid phase. And the comparison of structures in the ground state (grey) and excited state (green). **g**, Schematic representation in photophysical potential surface of bended intramolecular charge transfer state (BICT). M062X calculated geometries of the S_0, S_1, MECI and simulated energy profiles along the constructed LIIC pathways between the optimized S_1 and MECI geometries of TAO-TP*p*M. **h**, The plot of fluorescent peak intensity of TAO-TPMS, TAO-TP*o*M, TAO-TP and TAO-TP*p*M.

Aiming to elaborate the dynamic evolution of energy dissipation and molecular bending behaviors, S_0/S_1 minimal energy conical intersection (MECI) of TAO-TP*p*M was subsequently calculated by optimizing the geometries at the XMS-CASPT2//SA2-CASSCF(8,8)/cc-pVDZ level[42-44]. The constructed linearly interpolated internal coordinate (LIIC) pathways were constructed between the optimized S_0 and S_1, as well as S_1 and MECI. The energy profiles were computed along the LIIC pathways with XMS-CASPT2//SA2-CASSCF(12,12)/ cc-pVDZ. As illustrated in Fig 3g, the optimized S_0 geometry of TAO-TP*p*M possessed almost planar central ring with a dihedral angle of about 0.47° which was in good accordance with that in the crystal (0.24°) (Supplementary Table 6 and Fig. 9-10). Upon photoexcitation, both the optimized S_1 and MECI geometries exhibited a strong bending along the D-A charges divide of central ring giving large dihedral angles of 24.07° and 44.67°, respectively. Although the energy of S_1 state is directly uphill from the optimized geometries of S_1 to MECI, the energy of MECI is only larger than that of S_1-min by approximately 3.0 kcal/mol, indicating that the MECI is easily reached. It seems reasonable to infer that these presented mesoionic TAOs emit light through a new mechanism termed as bended intramolecular charge transfer (BICT). The BICT process enables TAOs to show both long emission wavelength and vanished fluorescence efficiency in the molecularly dissolved state, while the non-radiative decay was able to be efficiently suppressed via restriction of the bend in the central ring by aggregates formation, consequently offering significantly boosted emission intensity in the aggregation state.

In order to further verify this mechanism, the fluorescence properties of TAOs were measured in THF/water mixture with different water fractions (Fig. 3h). It was demonstrated that TAOs showed fluorescence intensity decrease when the fraction of water in high polarity was increased in the range of 10% to 80%, indicating strong BICT effect. Continuous raising water faction to over 80% led to the formation of aggregates, in which the bending of central ring and other intramolecular motions can be restricted to suppress the non-radiation decay, giving remarkably amplified emission. Nevertheless, in the cases of TAO-*o*M and TAO-TPMS, the constant reduction of fluorescence efficiency can be attributed to the bulky groups, which perhaps simultaneously hindered both those intramolecular motions in single molecule state and intense molecular packing in aggregate state. Eventually, BICT effect dominated their photophysical process against AIE effect in aggregates.

TAOs towards molecular transistor for the regulation of optical properties

Evaluation of structure-function relationships of TAOs was carried out by experiments and theoretical calculations. We first checked the viscosity effect on emission[45]. The emission intensity exhibited linear increase with raising the glycerol fraction from 0 to 90% (Fig. 4a and Supplementary Fig. 11). Moreover, the emission behavior of TAOs without bulky substituent group was more sensitive to environmental viscosity than that of their counterparts with bulky substituent group, which was determined by the slope comparison as shown in Fig. 4a. Analysis on their optimized geometries and charge distribution in S_0 and S_1 calculated by using M062X/6-31G (d, p) basis set demonstrated that stronger steric hindrance could result in more twisted conformation of ring Ⅲ with larger dihedral angle ($\theta_{Ⅲ}$) in S_0, less bending of central ring with larger dihedral angle (θ_{core}) upon excitation, and smaller changes in $\theta_{Ⅲ}$ from S_0 to S_1 (Fig. 4b, Supplementary Fig. 12 and Table 8). Combining these results, steric effect of ring Ⅲ mainly influenced the molecular motions especially the ring-bending in the solution to regulate the optical properties. The electronic effect of ring Ⅲ was then investigated. It was revealed that the absorption and emission wavelengths underwent red-shift with the gradual enhancement of electron-withdrawing effect, which was

in good accordance with the HOMO-LUMO energy gap outcomes (Fig. 4c-d and Supplementary Table 7). Evidently, in this presented mesoionic system, accompanying with efficient charge transfer from the D to A moiety, ring Ⅲ acted as a modulator to regulating fluorescence intensity and wavelength of TAOs, suggesting an ideal molecular transistor model as represented in Figure 4e.

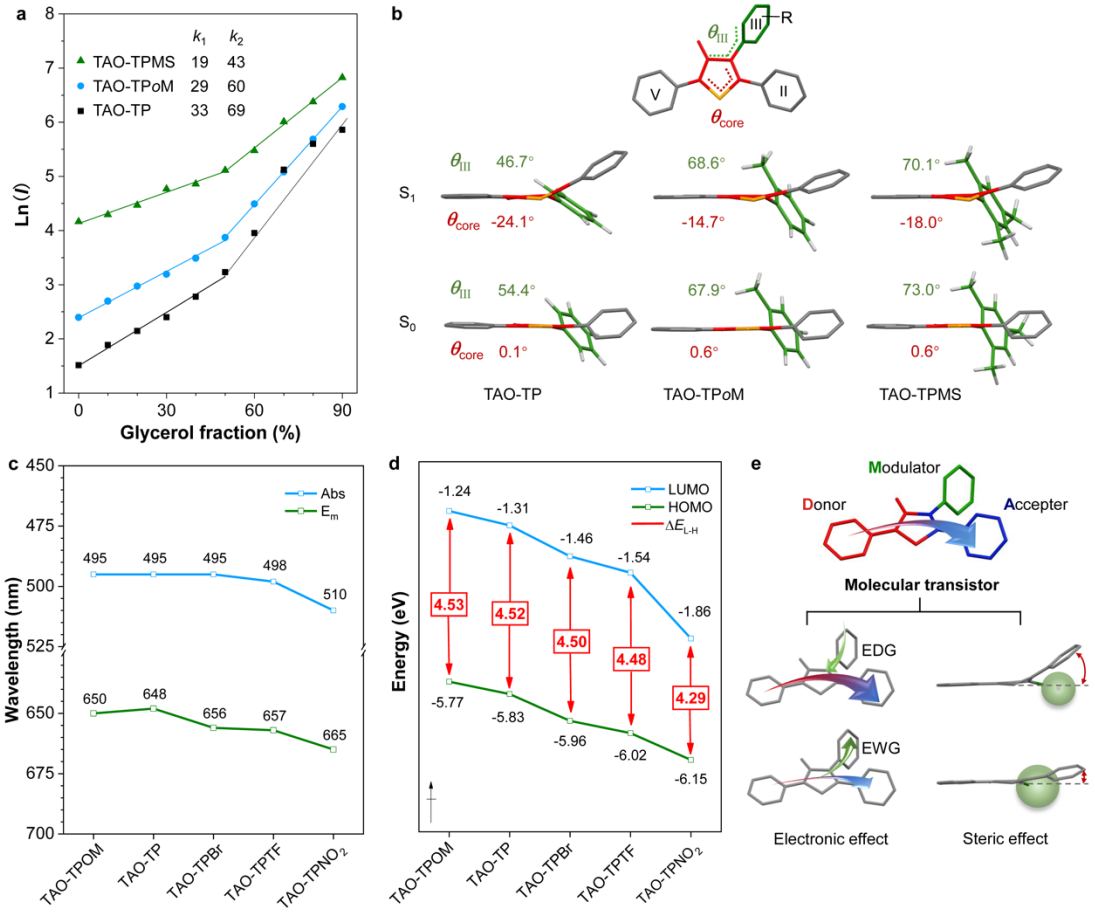

Figure 4. Molecular transistor of TAOs for fluorescent regulation. a, PL peak intensity of TAO-TP, TAO-TP*o*M and TAO-TPMS (2×10^{-5} M) in MeOH/glycerol mixtures with different glycerol fractions (f_w). **b**, The dihedral angles (θ_{III}, θ_{core}) of TAO-TP, TAO-TP*o*M and TAO-TPMS in the ground state and excited state calculated by using the M062X/6-31G (d, p) basis set. **c**, Plots of the maximum wavelengths of absorption and emission of TAOs. **d**, Plots of HOMO, LUMO energy levels and the energy gap ($\Delta E_{L\text{-}H}$) between HOMO and LUMO of TAOs calculated by using the M062X/6-31G (d, p) basis set. **e**, Schematic representation of electronic effects of molecular transistor.

Bioimaging of TAOs in living system

Luminogens with efficient red/NIR-emission have attracted great attentions as fluorescence probes in living system due to large penetration depth, low background antofluorescence and slight irradiation harm to tissues. Inspired by the good biocompatibility (Fig. 5b) and the AIE-active long-wavelength emission of TAOs, *in vitro* and *in vivo* bioimaging studies involving cell, bacteria and mouse brain were conducted. Taking TAO-TP as a representative, as illustrated in Fig. 5a and Supplementary Fig. 13, lysosome of cells can be clearly visualized with excellent image contrast to the cell background, and the imaging of TAO-TP and a commercially available lysosome tracker (LysoTracker) perfectly overlapped with as high as 92.6% of Pearson's correlation coefficient, indicating the high specificity for lysosome-staining. Various cell lines including HeLa, NIH 3T3, COS-7 and bEnd.3 were utilized for confirming the

lysosome-targeting ability of TAO-TP (Supplementary Fig. 14-16). And the photostability of TAO-TP dramatically outperformed LysoTracker (Fig. 5c and Supplementary Fig. 17). Moreover, this imaging protocol was further successfully extended to both Gram-negative and positive bacteria imaging, giving supremely high signal-to-noise ratio (Supplementary Fig. 18-19). The excellent imaging output could be benefited from the low molecular weight (MV~329 g·mol^{-1}) and suitable lipophilicity (the calculated log *P* = 4.8) of TAO-TP.

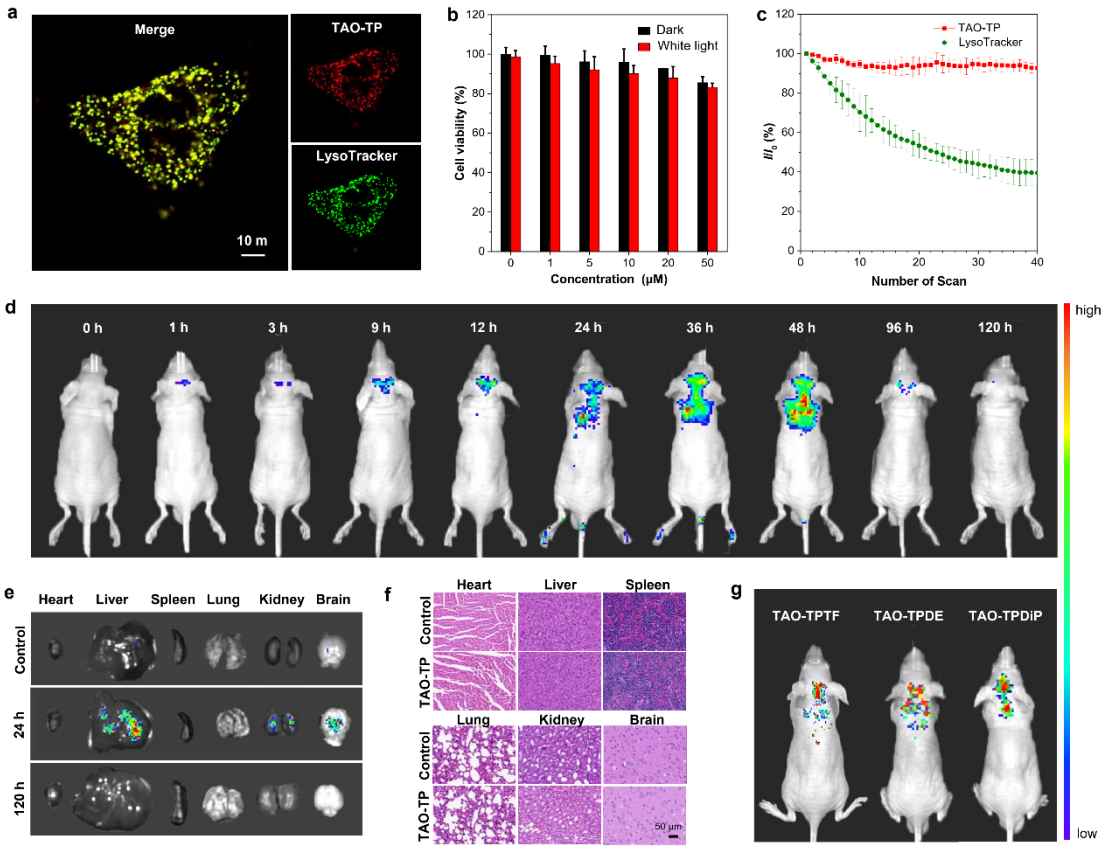

Figure 5. Biocompatible imaging of TAOs. a, Co-localization imaging of HeLa cells stained with LysoTracker Green and TAO-TP. λ_{ex} = 488 nm (3% laser power). Concentrations: TAO-TP (1 μM), LysoTracker Green (1 μM). The colocalization plot of LysoTracker Green and TAO-TP (Pearson's correlation coefficient: 92.6%). **b**, Cell viability of HeLa cells stained with different concentrations of TAO-TP in the absence or presence of white light irradiation. **c**, Loss in fluorescence of HeLa cells stained with TAO-TP and LysoTracker Green with the number of scans of laser irradiation. **d**, *In vivo* living imaging of BALB/c mice at different time points (0-120 h) before and after intravenous injection of TAO-TP (2.0 mg·kg^{-1}). (λ_{ex} = 500 nm, λ_{em} = 660 nm). **e**, *Ex vivo* fluorescence imaging of tissues (tumor, heart, liver, spleen, lung, kidney and brain) at 24 h and 120 h post-injection. **f**, Pathological analysis of the H&E-stained main organs sections of normal mice treated with PBS and TAO-TP (2.0 mg·kg^{-1}). **g**, *In vivo* living imaging of BALB/c mice at proper time after intravenous injection of TAO-TPTF, TAO-TPDE and TAO-TPDiP (2.0 mg kg^{-1}).

Additionally, it was found that the physicochemical properties of TAO-TP indeed met the rigorous requirements to assess the blood-brain barrier (BBB) penetrability, in terms of MV (<450), log *P* (1-5), polar surface area (PSA<80 Å^2) and hydrogen-bond donors (HBD<3)[46,47]. Expectedly, TAO-TP is capable of penetrating BBB to achieve brain imaging of mouse. Experimental research demonstrated

that fluorescence can be detected in brain at 1 h intravenous postinjection of TAO-TP (2.0 mg·kg^{-1}), and arrived maximum at 48 h postinjection (Fig. 5d). Subsequently, the signal stepwisely declined afterward to be undetected at around 120 h postinjection because of the metabolism. In order to further assess the biodistribution of TAO-TP, *ex vivo* fluorescence images of various organs were obtained at 24 h and 120 h postinjection, which confirmed the *in vivo* imaging results (Fig. 5e). Hematoxylin and eosin (H&E) staining of organ slices revealed the good biocompatibility of TAO-TP (Fig. 5f). Furthermore, fluorescence living imaging of the brain was also successfully realized by employing other TAO derivatives, such as TAO-TPTF, TAO-TPDE and TAO-TPDiP (Fig. 5g and Supplementary Fig. 20). These results indicated that TAOs were potentially powerful as versatile fluorescent probes for bioimaging, of particular towards brain imaging.

In conclusion, we developed a novel family of Janus luminogens with aggregation-induced red/NIR emission, namely TAOs, on the basis of mesoionic skeleton. These unique five-membered heterocycles featured an unprecedented D-A structure with high strength in a single ring and possessed inherent advantages including facile synthesis, adjustable structure and fine π-conjucation, endowing them with significant charge separation and transport. Combining QM/MM simulations and the excited state decay pathway simulations, we proposed BICT as a new mechanism to in-depth understanding the distinctive optical properties, and figured out that the AIE tendency was benefited from supremely suppressed non-radiation decay caused by efficient restriction of ring-bending and rotations. It was also found that the substitution at 3-position plays a critical role as modulator to modulate the optical properties, which makes TAOs potentially useful towards molecular transistor. In addition, TAOs well performed as fluorescent bioprobes sharing negligible toxicity, high photostability and excellent image contrast for visualizing cells and bacteria, especially for living brain benefiting from their appropriate physicochemical properties for BBB penetrability. The pioneering and comprehensive studies on TAOs provide significant insights for the development and structural regulation of novel mosoionic luminogens with advanced optoelectronic performance. More applications are being anticipated in molecular transistor device, and long-term bioactive molecule tracking and pathological research related cerebral disease diagnosis such as Alzheimer's disease, glioma and encephalitis.

Methods

Materials and instruments. All the chemicals and biological reagents for synthesis and analysis were purchased from Energy, Bide and Sigma-Aldrich Chemical Reagent Ltd., and used without further purification unless specified requirement. Nuclear magnetic resonance (NMR) spectra were measured on Bruker AVANCE III 400MHZ and 500MHZ NMR spectrometers. High resolution mass spectrometer (HRMS) was tested on Thermo Exactive Focus Q. UV-vis absorption spectra were measured on a PerkinElmer Lambda 950 spectrophotometer and SHMADZU UV-2450 UV-vis spectrophotometer. Fluorescence spectra were recorded on Edinburgh FS5 fluorescence spectrophotometer. Quantum yield was determined by a HAMAMATSU C11347 Quantaurus-QY plus. The theoretical calculations were performed with the Gaussian 09 program. Fluorescence images were collected on a confocal laser scanning microscope (CLSM, ZEISS-LSM880) and analyzed by using ZEN 3.2 software. *In vivo* fluorescence imaging was performed at Perknelmer IVIS Spectrum.

Synthesis of TAOs. In a dried screw cap tube, substituted N-phenylbenzothioamides (0.6 mmol, 1 eq.) and *α*-bromophenylacetyl chloride (140 mg, 0.6 mmol, 1 eq.) were stirred for 1 hour at room temperature

in dry toluene (3 mL). Then trimethylamine (164 μL, 1.20 mmol, 2 eq.) was added and the reaction mixture was stirred overnight at room temperature. The solvent was evaporated under vacuum and the crude product was extracted with dichloromethane and water. The combined organic layers were dried over magnesium sulfate and evaporated under vacuum. The desired product was purified by column chromatography (ethyl acetate/dichloromethane 1:4) and obtained by recrystallization as a powder.

Single crystal of TAO-TPpM. A suitable crystal of TAO-TP*p*M was obtained by solvent evaporation and tested on a SuperNova, Dual, Cu at home/near, Atlas diffractometer. The crystal was kept at 100.00(10) K during data collection. The deposition number 1935601 was provided free of charge by the joint Cambridge Crystallographic Data Centre and Fachinformationszentrum Karlsruhe Access Structures service www.ccdc.cam.ac.uk/structures.

Theoretical calculations. The geometries of isolated TAOs in the ground state (S_0) and the first excited state (S_1) were optimized using Gaussian 09 at M062X/6-31G (d, p) level. The electronic structure of TAO-TPpM was evaluated with the combined quantum mechanics and molecular mechanics (QM/MM) method using the ONIOM model in Gaussian 16 package. We constructed the ONIOM model by cutting a cluster containing 31 TAO-TP*p*M molecules. The central molecule was treated as the QM part at (TD)M062X/6-31G(d) level and the surrounding ones acted as the MM part with the universal force field (UFF). All the structures at the lowest energy point were confirmed by calculating the analytical frequency. Then the electron-vibration analysis was performed in the MOMAP package. The geometries of S_0, S_1, and MECI between S_0 and S_1 ($MECI_{S0/S1}$) were firstly optimized with the equal-weight, two-root (S_0, S_1) state-averaged (SA2) complete-active-space self-consistent-field (CASSCF) method. M062X calculated geometries of the S_0, S_1, MECI and XMS-CASPT2//SA2-CASSCF (12,12)/cc-pVDZ computed energy profiles along the constructed LIIC pathways between the optimized S_1 and MECI geometries of TAO-TP*p*M.

Bioimaging experiments.

Cell viability assay. All cell viability tests were evaluated by MTT assay in HeLa cells. Briefly, cancer cells were seeded in 96-well culture plate at a density of 6×10^4 cells per well incubated with DMEM/RPMI-1640 medium for 24 h. Then the medium was replaced by DMEM/RPMI-1640 containing TAO-TP with a series of concentrations. Afterwards, cells were incubated for another 12 h, or 24 h, or 48 h. MTT solution (5 mg/mL in PBS) was added as 10 μL per well, followed by another incubation for 4 h. All the mediums were removed and 150 μL DMSO was added. Cell viability was assessed by the measurement of the absorbance at 570 nm by microplate reader (BioTek). The relative cell viability was calculated by the equation: cell viability (%) = $(OD_{treated}/OD_{control}) \times 100\%$.

Cell imaging by confocal laser scanning microscope (CLSM, ZEISS-LSM880). The HeLa cells, NIH 3T3 cells and COS-7 cell (5×10^4 cells mL^{-1}) were seeded in confocal dishes and incubated for 24 h. TAO-TP (1 μM) was incubated with the cells for 30 min. After the removal of TAO-TP, the cells were washed three times with PBS, and LysoTracker Green (1 μM) was incubated with the cells for 30 min. The imaging of the cells was recorded by a CLSM. TAO-TP: E_x = 488 nm, E_m = 550-740 nm; LysoTracker Green: E_x = 488 nm, E_m = 500-550 nm.

Bacteria staining. 500 μM bacteria (OD600=1.0) in a 1.5 mL centrifuge tube were harvested by centrifuging. Then the supernatant was removed, 50 μL of 1, 5,10 μM TAO-TP in PBS solutions were added, and incubated for 20 min at room temperature. 2 μL of the stained bacteria solution was transferred to a glass slide, and covered by a coverslip for imaging. The images of *E.coli* and *S. aureus* were captured by a CLSM. TAO-TP: E_x = 488 nm, E_m = 550-740 nm.

***In vivo* imaging and biosafety study.** Experiment protocols involving animals were authorized by the Laboratory Animal Center of Shenzhen Graduate School Peking University. BALB/c male nude mice (4 weeks of age) was purchased from Beijing Vital River Laboratory Animal Technology. Mice were intravenously injected via tail vein with 200 μL of TAOs (2.0 mg kg^{-1}), mice without any treatment were used as negative control. The *in vivo* fluorescence intensity was monitored at different time points after intravenous injection by using PerkinElme IVIS Spectrum In-Vivo imaging system (E_x = 500 nm, E_m = 660 nm). For study the biodistribution profiles of TAOs, mice were sacrificed by cervical vertebra dislocation at 12, 24 and 72 h, eventually the heart, liver, spleen, lung, kidney and brain were taken from the mice. The main organs (heart, liver, spleen, lung, kidney and brain) were carried out *ex vivo* imaging and stained with H&E for the histological section.

References:

1 Uoyama, H., Goushi, K., Shizu, K., Nomura, H. & Adachi, C. Highly efficient organic light-emitting diodes from delayed fluorescence. *Nature* **492**, 234-238 (2012).

2 Liu, Y., Li, C., Ren, Z., Yan, S. & Bryce, M. R. All-organic thermally activated delayed fluorescence materials for organic light-emitting diodes. *Nat. Rev. Mater.* **3**, 18020 (2018).

3 Zaumseil, J. Recent developments and novel applications of thin film, light-emitting transistors. *Adv. Funct. Mater.* **30**, 1905269 (2019).

4 Li, H. et al. Chemical and biomolecule sensing with organic field-effect transistors. *Chem. Rev.* **119**, 3-35 (2019).

5 Ning, Z., Fu, Y. & Tian, H. Improvement of dye-sensitized solar cells: What we know and what we need to know. *Energy Environ. Sci.* **3**, 1170-1181 (2010).

6 Wadsworth, A. et al. Critical review of the molecular design progress in non-fullerene electron acceptors towards commercially viable organic solar cells. *Chem. Soc. Rev.* **48**, 1596-1625 (2019).

7 Kwok, R. T. K., Leung, C. W. T., Lam, J. W. Y. & Tang, B. Z. Biosensing by luminogens with aggregation-induced emission characteristics. *Chem. Soc. Rev.* **44**, 4228-4238 (2015).

8 Wu, D. et al. Fluorescent chemosensors: the past, present and future. *Chem. Soc. Rev.* **46**, 7105-7123 (2017).

9 Ostroverkhova, O. Organic optoelectronic materials: Mechanisms and applications. *Chem. Rev.* **116**, 13279-13412 (2016).

10 Roncali, J. Synthetic principles for bandgap control in linear π-conjugated systems. *Chem. Rev.* **97**, 173-206 (1997).

11 Wang, C., Dong, H., Hu, W., Liu, Y. & Zhu, D. Semiconducting π-conjugated systems in field-effect transistors: A material odyssey of organic electronics. *Chem. Rev.* **112**, 2208-2267 (2012).

12 Bronstein, H., Nielsen, C. B., Schroeder, B. C. & McCulloch, I. The role of chemical design in the performance of organic semiconductors. *Nat. Rev. Chem.* **4**, 66-77 (2020).

13 Bakulin, A. A. *et al.* The role of driving energy and delocalized states for charge separation in organic semiconductors. *Science* **335**, 1340-1344 (2012).

14 Savoie, B. M., Jackson, N. E., Chen, L. X., Marks, T. J. & Ratner, M. A. Mesoscopic features of charge generation in organic semiconductors. *Acc. Chem. Res.* **47**, 3385-3394 (2014).

15 Hutchison, G. R., Ratner, M. A. & Marks, T. J. Intermolecular charge transfer between heterocyclic oligomers. Effects of heteroatom and molecular packing on hopping transport in organic semiconductors. *J. Am. Chem. Soc.* **127**, 16866-16881 (2005).

16 Deibel, C., Strobel, T. & Dyakonov, V. Role of the charge transfer state in organic donor-acceptor solar cells. *Adv. Mater.* **22**, 4097-4111 (2010).

17 Chochos, C. L. & Choulis, S. A. How the structural deviations on the backbone of conjugated polymers influence their optoelectronic properties and photovoltaic performance. *Prog. Polym. Sci.* **36**, 1326-1414 (2011).

18 Zhang, W., Liu, Y. & Yu, G. Heteroatom substituted organic/polymeric semiconductors and their applications in field-effect transistors. *Adv. Mater.* **26**, 6898-6904 (2014).

19 Hou, J., Inganas, O., Friend, R. H. & Gao, F. Organic solar cells based on non-fullerene acceptors. *Nat. Mater.* **17**, 119-128 (2018).

20 Zampetti, A., Minotto, A. & Cacialli, F. Near-infrared (NIR) organic light-emitting diodes (OLEDs): Challenges and opportunities. *Adv. Funct. Mater.* **29**, 1807623 (2019).

21 Wu, Y. & Zhu, W. Organic sensitizers from D-π-A to D-A-π-A: effect of the internal electron-withdrawing units on molecular absorption, energy levels and photovoltaic performances. *Chem. Soc. Rev.* **42**, 2039-2058 (2013).

22 Ying, L., Huang, F. & Bazan, G. C. Regioregular narrow-bandgap-conjugated polymers for plastic electronics. *Nat. Commun.* **8**, 14047 (2017).

23 Cheng, P., Li, G., Zhan, X. & Yang, Y. Next-generation organic photovoltaics based on non-fullerene acceptors. *Nat. Photonics* **12**, 131-142 (2018).

24 Wan, X., Li, C., Zhang, M. & Chen, Y. Acceptor-donor-acceptor type molecules for high performance organic photovoltaics – chemistry and mechanism. *Chem. Soc. Rev.* **49**, 2828-2842 (2020).

25 Xu, S., Duan, Y. & Liu, B. Precise molecular design for high-performance luminogens with aggregation-induced emission. *Adv. Mater.* 32, 1903530 (2020).

26 Baker, W., Ollis, W. D. & Poole, V. D. Cyclic meso-ionic compounds. 1. The structure of sydnones and related compounds. *J. Chem. Soc.* 307-314 (1949).

27 Baker, W. & Ollis, W. D. Meso-ionic compounds. *Q. Rev. Chem. Soc.* **11**, 15-29 (1957).

28 Bernard, S. *et al.* Bioorthogonal click and release reaction of iminosydnones with cycloalkynes. *Angew. Chem. Int. Ed.* **56**, 15612-15616 (2017).

29 Ji, X. *et al.* Click and release: Bioorthogonal approaches to "on-demand" activation of prodrugs. *Chem. Soc. Rev.* **48**, 1077-1094 (2019).

30 Porte, K. *et al.* Controlled release of a micelle payload via sequential enzymatic and bioorthogonal reactions in living systems. *Angew. Chem. Int. Ed.* **58**, 6366-6370 (2019).

31 Ollis, W. D. & Ramsden, C. A. Meso-ionic Compounds. *Adv. Heterocycl. Chem.* **19**, 1-122 (1976).

32 Marder, S. R. et al. Large first hyperpolarizabilities in push-pull polyenes by tuning of the bond length alternation and aromaticity. *Science* **263**, 511-514 (1994).

33 DeOliveira, M. B. *et al.* Mesoionic 2-*N*-cycloalkylamino-5-alkyl-1,3-dithiolium-4-thiolates. *Phosphorus. Sulfur. Silicon. Relat. Elem.* **108**, 75-84 (1996).

34 Luo, J. *et al.* Aggregation-induced emission of 1-methyl-1,2,3,4,5-pentaphenylsilole. *Chem. Commun.* 1740-1741 (2001).

35 Weiss, J. Fluorescence of organic molecules. *Nature* **152**, 176-178 (1943).

36 Mei, J., Leung, N. L., Kwok, R. T., Lam, J. W. & Tang, B. Z. Aggregation-induced emission: Together we shine, united we soar! *Chem. Rev.* **115**, 11718-11940 (2015).
37 Zhang, H. *et al.* Aggregate science: From structures to properties. *Adv. Mater.* **32**, 2001457 (2020).
38 Zhao, Z., Zhang, H., Lam, J. W. Y. & Tang, B. Z. Aggregation-induced emission: New vistas at the aggregate level. *Angew. Chem. Int. Ed.* **59**, 9888-9907 (2020).
39 Nigam, S. & Rutan, S. Principles and applications of solvatochromism. *Appl. Spectrosc.* **55**, 362A-370A (2001).
40 Zhang, T. *et al.* Aggregation effects on the optical emission of 1,1,2,3,4,5-hexaphenylsilole (HPS): A QM/MM study. *J. Phys. Chem. A* **118**, 9094-9104 (2014).
41 Shuai Z., Peng Q. Organic light-emitting diodes: theoretical understanding of highly efficient materials and development of computational methodology. *Nat. Sci. Rev.* **4**, 224-239 (2017).
42 Granovsky, A. A. Extended multi-configuration quasi-degenerate perturbation theory: The new approach to multi-state multi-reference perturbation theory. *J. Chem. Phys.* **134**, 214113 (2011).
43 Vlaisavljevich, B. & Shiozaki, T. Nuclear energy gradients for internally contracted complete active space second-order perturbation theory: Multistate extensions. *J. Chem. Theory. Comput.* **12**, 3781-3787 (2016).
44 Zhou, P., Li, P., Zhao, Y. & Han, K. Restriction of flip-flop motion as a mechanism for aggregation-induced emission. *J. Phys. Chem. Lett.* **10**, 6929-6935 (2019).
45 Chen, J. *et al.* Synthesis, light emission, nanoaggregation, and restricted intramolecular rotation of 1,1-substituted 2,3,4,5-tetraphenylsiloles. *Chem. Mater.* **15**, 1535-1546 (2003).
46 Hitchcock, S. A. & Pennington, L. D. Structure-brain exposure relationships. *J. Med. Chem.* **49**, 7559-7583 (2006).
47 Li, D., Edward, H. K. & Guy, T. C. Drug-like property concepts in pharmaceutical design. *Curr. Pharm. Design* **15**, 2184-2194 (2009).

Acknowledgements

This work was partially supported by the Natural Science Foundation of China (21907068, 21801169), the Natural Science Foundation for Distinguished Young Scholars of Guangdong Province (2020B1515020011), and the Science and Technology Foundation of Shenzhen City (JCYJ20190808153415062, RCYX20200714114525101). The authors also acknowledge the Instrumental Analysis Center of Shenzhen University.

Author contributions

Q.W. and D.W. designed the experiments. Q.W. was responsible for materials design, synthesis and characterization and manuscript preparation. J.L. and L.R. contributed mechanistic study and theoretical calculation. P.Z. contributed theoretical calculation of MECI. Q.W., Y.L. and M.M.S.L. carried out all bioimaging and related biological experiments. Q.W., D.W. and B.Z.T. discussed the results and drafted the manuscript. All authors contributed to the proofreading of the manuscript.

Competing interests

The authors declare no competing interests.

Additional information

Supplementary information accompanies this paper on www.nature.com/naturematerials.